

Solvent Selectivity Governed Self-assembly of Block Copolymer in Nanofabrication

Guoxing Liao,^{#,1,2} Lei Chen,^{#,1,3} Yunjie Zhang,¹ Oleksandr O. Mykhaylyk,² Paul D. Topham,⁴ Daniel T. W. Toolan,² Matthew J. Derry,⁴ Jonathan R. Howse,⁵ Qianqian Yu,¹ Guiju Feng,¹ LinGe Wang^{1,*}

¹. South China Advanced Institute for Soft Matter Science and Technology, School of Emergent Soft Matter, Guangdong Provincial Key Laboratory of Functional and Intelligent Hybrid Materials and Devices, South China University of Technology, Guangzhou, 510640, China.

². Department of Chemistry, University of Sheffield, Brook Hill, Sheffield, S3 7HF, UK.

³. Guangzhou Haige Communications Group Incorporated Company, Guangzhou 510663, China.

⁴. Aston Advanced Materials Research Centre, School of Infrastructure and Sustainable Engineering, College of Engineering and Physical Sciences, Aston University, Birmingham, B4 7ET, UK.

⁵. Department of Chemical and Biological Engineering, Mappin Street, Sheffield, S1 3JD, UK.

[#] Liao and Chen contributed equally to the work.

^{*} Corresponding authors: lingewang@scut.edu.cn (L. G. Wang).

ABSTRACT

Block copolymer-based nanoproducts including particles, fibers and films show promise in high-end applications including nanotemplating, nanolithography, and nanoporous membranes due to their advantageous self-assembled structure. However, few studies probe the nanofabrication process in detail and monitor the concomitant self-assembled structural transitions. Herein, time-resolved small-angle X-ray scattering (SAXS) is exploited to follow such

nanostructural changes. Evaporation-induced casting, electrospraying or electrospinning, followed by a final solvent vapor annealing step, have been used to create a series of nanoproducts with reversibly tunable morphologies from a model block copolymer, polystyrene-*b*-poly(ethylene-*co*-butylene)-*b*-polystyrene (SEBS). During evaporation-induced casting, which is considered as an unconfined system, a selective (co)solvent system composed of tetrahydrofuran (THF) and dimethylformamide (DMF) can lead to the formation of various SEBS structures. For DMF-based unconfined systems, the final SEBS lamellar structures were found to be different from the structure formed from THF only, demonstrating the critical role of solvent selection in evaporation-induced casting. The comparison of SEBS electrospun fibers reveals the unique and complex self-assembled structural transition occurring in a confined system. Time-resolved SAXS studies of our model triblock copolymer provide guidelines for a more general approach to access various nanostructures from self-assembling block copolymers.

Keywords

Self-assembly, Block copolymers, Nanofabrication, Time-resolved SAXS

1. Introduction

Self-assembled block copolymers (BCPs) provide a powerful platform to tailor, template and control systems with well-ordered nanofeatures for bottom-up nanofabrication, and have received great interest for approximately the past five decades [1-4]. The ability to manipulate molecular composition and thus resultant morphology has led to BCP-based nanoproducts being utilized for electronics [5, 6], biotechnology [7] and nanoscale lithographical applications [8] [9], amongst

others. Studies of the nanoscale morphology and architecture that can be fabricated using BCPs have been widely reported [2, 10-13]. For example, BCP thin films with sub-100 nm thickness [14, 15] and electrospun BCP fibers with high surface area-to-volume ratio and controlled surface morphology [16, 17] have been explored. In these reports, not only were the fabrication methods described, but the post-processing treatment and feature geometries of tailored BCP nanoproducts were also highlighted [18], demonstrating the importance that processing plays in realizing and achieving the BCP structure prescribed within its molecular chain structure.

Since BCPs are made up of chemically distinct polymer segments that are joined together by covalent bonds [2], they can self-assemble into a wide range of ordered shapes, including spheres, gyroids, cylinders, and lamellae [19]. Notably, the different polymer segments within BCPs can have varying interactions with solvents, depending on the chemical structure of the monomeric building blocks [20, 21]. Selective solvents (including solvent vapor) can act as plasticizers for one or more of the blocks within a BCP, reducing their glass transition temperature (T_g) below room temperature and increasing the mobility of these blocks. Induced by selective solvents, BCP structural rearrangements have been observed in solution, particles, fibers, and thin films [22-24]. Combining membrane emulsification and solvent annealing processes, polystyrene-*b*-poly(1,4-butadiene) (PS-*b*-PB) [25], polystyrene-*b*-polydimethylsiloxane (PS-*b*-PDMS) [26], and polystyrene-*b*-poly(4-vinylpyridine) (PS-*b*-P4VP) [27] nanoproducts with controlled size, shape, and internal structure were prepared. Bulk amphiphilic polystyrene-*b*-poly(2-vinylpyridine) (PS-*b*-P2VP) [28] was soaked in ethanol at 70 or 75 °C to form three-dimensional perforated fibers, and the porosity increased with increasing degree of swelling. Polystyrene-*b*-poly(*N*-isopropylacrylamide)-*b*-polystyrene (PS-*b*-PNIPAM-*b*-PS) thin films with diverse, well-defined periodic nanostructures were observed during selective solvent annealing [29]. Solvents typically

do not pose any risk of polymer degradation and also provide the possibility of solvent selectivity for specific blocks within the BCP, which is a useful strategy to access non-equilibrium morphologies during BCP nanofabrication [20, 30, 31]. However, in such reports, very few studies [32] have probed the nanofabrication process in detail and monitored the concomitant self-assembled structural transitions.

Herein, in this study, polystyrene-*b*-poly(ethylene-*co*-butylene)-*b*-polystyrene (SEBS) films were produced via an evaporation-induced method in THF/DMF cosolvents within unconfined configurations. We wanted to use this model to investigate the nanofabrication process in detail and monitor the concomitant self-assembled structural transitions. The roles that the solvents play need to be considered in terms of both imparted mobility (enabling the polymer chains to achieve their predicted equilibrium structures), as well as their partitioning between mobile blocks, which influences the volume fractions of the blocks (where one block will be swollen more than the other in a selective solvent). SEBS films constructed under confined conditions were prepared using electrospun SEBS fibers. To observe the self-assembled SEBS film nanostructures, time-resolved small-angle X-ray scattering (SAXS), one of the most advanced and powerful characterization technologies for probing nanoscale features, was used to identify and monitor the potential face-centered cubic (FCC) and lamellar (LAM) self-assembled structures [33] and any associated structural transitions. SAXS modelling of these time-resolved SAXS data provides detailed information of the self-assembled structure of SEBS films prepared in both unconfined and confined conditions. For unconfined configurations, time-resolved SAXS measurements and modelling results can reveal the role of (co)solvent during the nanofabrication of triblock copolymer self-assembled structures. Moreover, for confined systems, SAXS can first reveal the confined nanostructures fabricated by the electrospinning method, and time-resolved SAXS can

be used to understand how the self-assembled structures evolve within the electrospun fibers during solvent vapor annealing (SVA). These time-resolved SAXS studies highlight the significant role of (co)solvent selection and the resultant effect on the self-assembled structure during nanofabrication in an unconfined system. In contrast, SAXS analysis of the nanostructures within the electrospun fibers provides valuable insights of the mechanism of self-assembled structural transitions in a confined system.

2. Experimental section

2.1. Materials

Triblock copolymer, polystyrene-*b*-poly(ethylene-*co*-butylene)-*b*-polystyrene (SEBS) (Kraton G1650, $M_w = 75.1$ kg/mol, polystyrene (PS) volume fraction $\phi = 0.30$), was obtained from Kraton Performance Polymers, Inc. Laboratory grade tetrahydrofuran (THF) and dimethylformamide (DMF) were purchased from Aladdin and used as received.

2.2. SEBS solution and thin film preparation

Triblock copolymer SEBS powder was dissolved in THF/DMF mixtures (from 100/0 to 0/100, w/w ratio, in 10% increments – 11 samples in total) at a total concentration of 14% w/w. All solutions were stirred overnight at 25 °C prior to use. SEBS solution was poured into a polytetrafluoroethylene (PTFE) mold (a PTFE ring with 8 mm inner diameter and 1 mm thickness) in a sample holder cell (**Fig. S1**) and the SEBS thin film was prepared by the evaporation-induced method at 25 °C until the stable SEBS thin film formed.

2.3. SEBS fiber/particle preparation and SVA treatment

Electrospinning/spraying experiments were performed using homemade apparatus described in previous reports [33, 34]. SEBS solutions at a total concentration of 14% w/w were drawn into a 1 mL syringe connected to a metallic needle and fed at 2 mL/h using a syringe pump (Aladdin-220, World Precision Instruments Ltd., USA). A high voltage supply (Genvolt-73030, Genvolt High Voltage Industries Ltd., UK) was connected to the metallic needle and fixed at 20 kV. The distance between the needle and collector was fixed at 15 cm. The collected SEBS fibers were dried in a vacuum oven at 60 °C for 24 h to remove any residual solvent. SVA treatment was performed using a custom-designed device [24].

2.4. Characterization

For time-resolved SAXS studies, SAXS patterns of SEBS films during the evaporation-induced method from SEBS solutions at 14% w/w in THF/DMF mixtures were recorded at 30 min intervals until no further change in the SAXS pattern was observed using a Bruker NanoStar Laboratory SAXS instrument equipped with a Cu K α radiation source ($\lambda = 1.54 \text{ \AA}$) and a 2D position-sensitive gas detector (Hi-Star, Siemens AXS). SAXS patterns were collected over a q range of 0.01 to 0.1 \AA^{-1} [$q = (4\pi/\lambda) \cdot \sin\theta$, where θ is half of the scattered angle and λ is X-ray radiation wavelength]. The (co)solvent of the deposited solutions evaporated during *in situ* SAXS measurements. The SEBS fibers were fixed in a sample chamber between Kapton windows with a thickness of 60 μm . The chamber was sealed during the SVA process to ensure that fibers were exposed to solvent vapor. Time-resolved SAXS measurements of SEBS electrospun fibers during THF vapor annealing have been described elsewhere [24]. Briefly, SAXS patterns were recorded every 133 seconds for 130 min using a Xeuss 2.0 laboratory SAXS instrument equipped with a liquid gallium

MetalJet-D2 X-ray source ($\lambda = 1.34 \text{ \AA}$) (Excillum, Stockholm, Sweden) and a Pilatus 1M hybrid pixel detector (Dectris, Baden, Switzerland). SAXS patterns were collected over a q range of 0.003 to 0.16 \AA^{-1} . 2D SAXS patterns were reduced (integrated and divided by the sample transmission coefficient) to 1D SAXS profiles using SAXSutilities software supplied by ESRF [35]. SAXS data analysis was performed using either Scatter [36] or Irena [37], a macro package for small-angle scattering (SAS) data analysis within the commercial Igor Pro software.

Gel permeation chromatography (GPC) was used to assess diblock copolymer molecular weight distributions using Agilent 1260 Infinity II LC System (Agilent Technologies, Santa Clara, United States). The GPC set-up comprised two $10 \mu\text{m}$ (30 cm) 'PLgel MIXED-B' columns and a G7162A refractive index detector. THF eluent purchased from Fisher Chemical (Waltham, United States) containing 0.02% v/v water and 0.015% w/v peroxide was used at a flow rate of $0.50 \text{ mL}\cdot\text{min}^{-1}$. A series of eight near-monodisperse linear polystyrene standards (M_w ranging from 162 to $6,545,000 \text{ g}\cdot\text{mol}^{-1}$) provided by Agilent Technologies were employed for calibration using the above refractive index detector.

The surface morphologies of the electrospun or electrosprayed SEBS samples were studied by scanning electron microscopy (SEM) using a JSM-7900F instrument operating at an accelerating voltage of 15 kV. Samples were mounted onto SEM studs using adhesive conducting pads and then gold-coated prior to analysis.

3. Results and discussion

3.1. Self-assembled structures of SEBS in solutions

Solvent-assisted polymer nanofabrication is an attractive method for functional material manufacturing as solvent-polymer interactions can be effectively used to tune processing conditions [38-41]. Herein, SEBS powders were dissolved in (co)solvent systems of THF and/or DMF, and the M_w and the relatively narrow molecular weight distribution of SEBS have been confirmed by GPC (**Fig. S2**). In this respect, the Hansen solubility parameters (HSPs) [42-44] could be employed to estimate the Flory-Huggins interaction parameters (χ) [45, 46] of DMF-PS, DMF-PEB, THF-PS, and THF-PEB pairs. Calculated by Eq S1, the χ values for PEB-PS, DMF-PS, DMF-PEB, THF-PS, THF-PEB were calculated to be 0.10, 0.55, 1.30, 0.14, and 0.37, respectively. These χ values indicate that PEB is incompatible with DMF than PS end-blocks, while THF is a good solvent for both PS and PEB blocks. Due to the different affinities of these blocks towards the two solvents, the turbidity of a series of SEBS solutions at 14% w/w for potential different degree of molecular chain entanglement could be observed by naked eye (**Fig. 1a**). As the amount of DMF in the solvent system increases, the homogeneous SEBS solution (THF/DMF = 100/0 w/w) gradually transforms into a gel (THF/DMF = 90/10 - 60/40 w/w), and then to a macrophase separated state (THF/DMF = 50/50 - 0/100 w/w) due to the poor affinity of DMF for the SEBS triblock copolymer. The extent of molecular entanglement in the SEBS solutions and gels on the 14% w/w (co)solvents was further confirmed by SAXS (**Fig. 1b and 1c**). There was no peak in the SAXS profile of SEBS solution with neat THF, indicating little or no aggregation of the polymer chains. Indeed, this SAXS pattern at THF/DMF = 100/0 w/w can be well-fitted to the diblock linear copolymer model [47] (**Fig. 1c**), revealing that the SEBS chains

behaved as Gaussian chains in solution. Introducing a small amount of DMF in the solvent system (THF/DMF = 90/10 w/w), a peak at $q = 0.019 \text{ \AA}^{-1}$ in the SAXS profile of this SEBS gel was observed, which highlights the structural transition of SEBS associated with the selectivity of DMF. However, this was the only peak observed indicating a possible packing of spheres with a short-range order. When the DMF content reached 20% w/w and 30% w/w, the resolved diffraction peaks had the relative q -positions of $1:\sqrt{8/3}:\sqrt{20/3}$, corresponding to (111), (022), and (024) faces of FCC structure [33] formed within the SEBS gel (**Fig. 1a**). The FCC lattice structure formed by possible PS spheres [33] has been estimated by a model developed by Förster et al. [48] (**Fig. 1c**). For THF/DMF = 80/20 w/w, the lattice period was 79.7 nm, while for THF/DMF = 70/30 w/w, the lattice period was 72.9 nm. The sphere radii of FCC for THF/DMF = 80/20 and 70/30 w/w were $16.5 \pm 2.6 \text{ nm}$ and $15.1 \pm 1.7 \text{ nm}$, respectively. The SAXS analysis and the hexagonal ‘six-spot’ patterns observed for THF/DMF = 80/20 w/w (**Fig. 1b**) indicated that the self-assembled SEBSs in such cosolvent form well-defined FCC structure. The closest PS sphere distances in the FCC structures were 23.4 nm and 21.3 nm for 80/20 and 70/30, respectively, which were both close to the end-to-end distance value of PEB blocks (R_{F_PEB}) when $\nu = 0.5$, where ν is the Flory exponent (see the Supporting Information). These also indicated that the PS blocks might form emulsions as the spheres of the FCC structures to capture DMF, which is incompatible with PEB blocks. Interestingly, FCC structures constructed by self-assembly of the block copolymers are rarely [49-54], because of the strong thermal fluctuations [55-57]. However, the low SEBS concentrations led to the weak interactions and the low level of overlap between the coronas (the PEB blocks) of the PS spheres [50, 58]. Meanwhile, the bridged configurations should be the dominant morphology of the ABA triblock copolymers [59], and therefore, the PS spheres were linked by the bridging PEB blocks to form FCC structures, rather typical BCC structures. When

the solvent system became increasingly bad for the PEB blocks (THF/DMF = 60/40 w/w and 50/50 w/w), a structural transition was observed, which was indicated by the formation of two broad peaks with their position ratio of $q^* : 2q^*$, possibly corresponding to a lamellar (LAM) phase. Indeed, a LAM structural model composed of the lamellar structure factor and the disk form factor [33] produced a good fit to the experimental data (**Fig. 1c**). These fitting results enabled determination of additional information about the formed nanostructures including the disk thickness (T), the lamellae inter-plane distance (D), and a relative mean square displacement for the LAM translational disorder (σ). The SAXS analysis indicated that D was 37.3 ± 1.9 nm in THF/DMF = 60/40 w/w and 38.9 ± 2.8 nm in THF/DMF = 50/50 w/w and T was 11.2 ± 2.9 nm in THF/DMF = 60/40 w/w and 12.5 ± 5.9 nm in THF/DMF = 50/50 w/w. The measured T values were both close to $4R_{g_PS}$ (= 11.5 nm) when $\nu = 0.5$ (see the estimation in Supporting Information), which indicated that the PS sublayers of the LAM phase were constructed of two PS coils with head-to-head configuration. The thickness of the PEB sublayer, calculated as $(D - T)$, was 26.1 nm and 26.4 nm for THF/DMF = 60/40 w/w and THF/DMF = 50/50 w/w solvent compositions, respectively, which were close to R_{F_PEB} (= 24.3 nm) when $\nu = 0.5$.

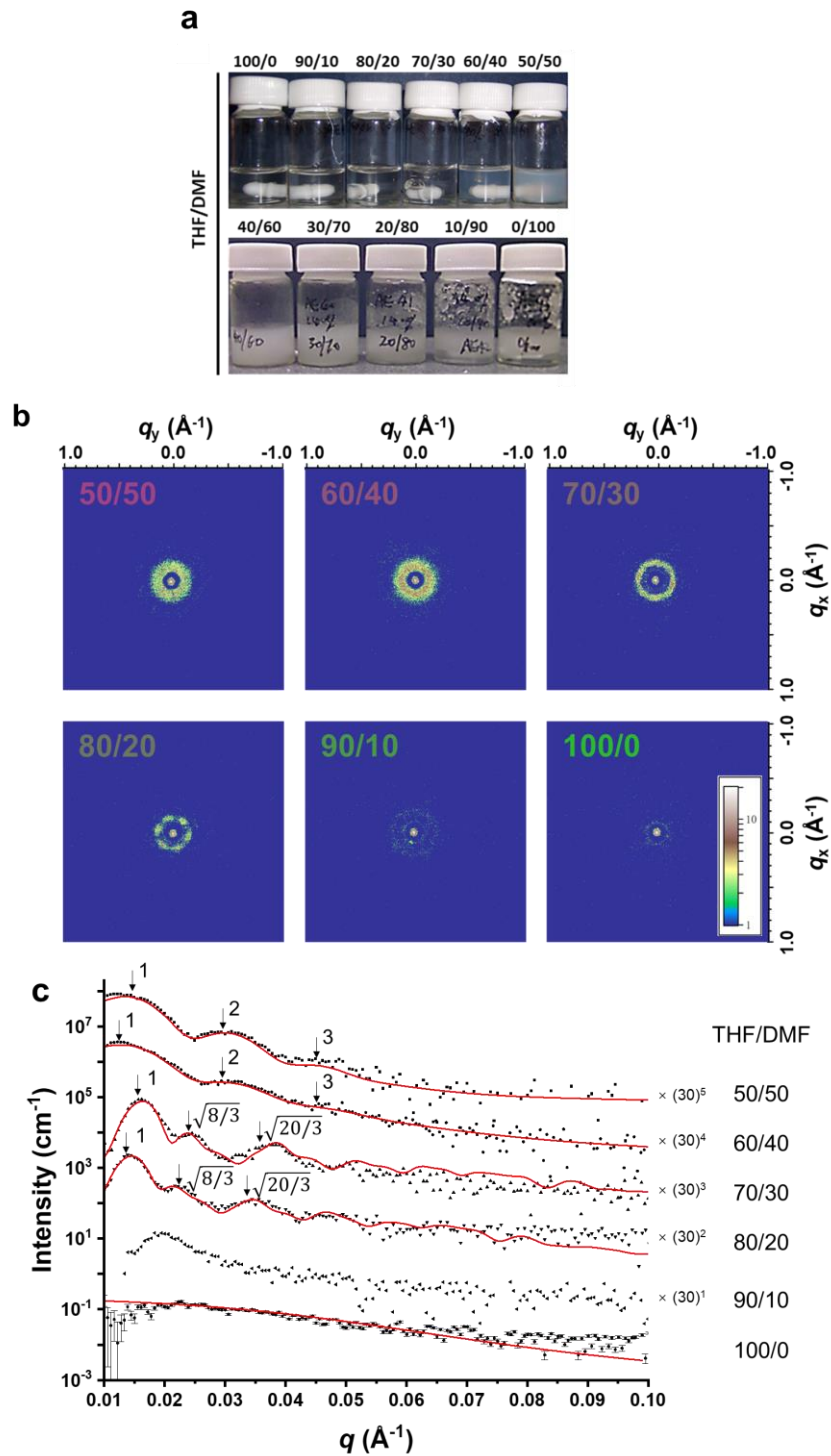


Fig. 1. Characterization of SEBS solutions or gels at 14% w/w in a solvent mixture with various THF/DMF ratio (w/w): (a) digital photos of prepared samples, (b) representative 2D SAXS patterns and (c) their corresponding 1D SAXS profiles. The resolved diffraction peaks are labeled

by their position (q/q^* ratio). For clarity purposes, the 1D SAXS patterns have been shifted upward by a multiplication factor indicated on the right side of the plot. Representative standard deviation bars are shown for the 1D SAXS pattern associated with THF/DMF = 100/0 w/w. Structural model fits to the 1D SAXS patterns are shown by the solid red lines.

3.2. Final products of self-assembled structures of SEBS in films via evaporation-induced method

After the preparation of stable SEBS films via the evaporation-induced method of various THF/DMF solutions when no further change in the SAXS pattern was observed, all SEBS films exhibited lamellae nanostructure, as confirmed by SAXS data showing clear peaks with the diffraction peak position ratio (q/q^*) of 1:2:3 (**Fig. 2a**). The LAM structural model was also employed here to analyze the LAM phase structure (**Fig. 2a** and **Fig. 2b**). It was found for THF/DMF = 100/0 w/w - 60/40 w/w solvent compositions that the PS sublayer thickness (T) was approximately 11 nm, which was close to $4R_{g_PS}$ when $\nu = 0.5$. These results indicated that the two PS coils with head-to-head configuration constructed such PS sublayers in all the studied solvent compositions including the final film of THF/DMF = 100/0 w/w (**Fig. 2c**). Meanwhile, the PEB sublayer thickness ($D - T$) for all solvent compositions containing DMF remained around 28 nm and dropped down to 24.2 nm for the final film with no DMF (THF/DMF = 100/0 w/w), which was close to R_{F_PEB} when $\nu = 0.5$ (**Fig. 2c**). However, the 28-nm PEB sublayers when containing DMF may be packed by SEBS chains in different configurations in a comparison with the 24-nm PEB sublayers. Considering that the length of such PEB sublayers approximately quadruples the radius of gyration of the folded PEB blocks ($4R_{g_PEB_folded} = 28.0$ nm) (see the estimation in Supporting Information), 28-nm PEB sublayers could likely to be constructed by two folded PEB coils with head-to-head configuration (**Fig. 2d**).

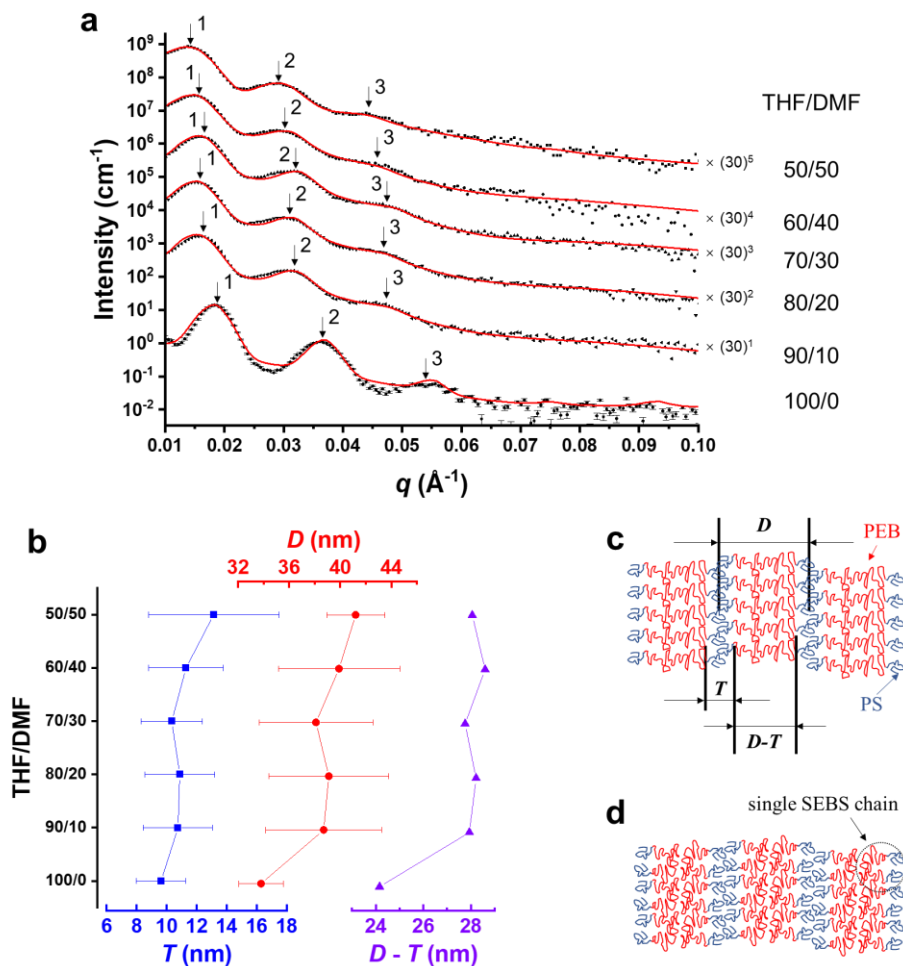


Fig. 2. SAXS characterization of SEBS films prepared by evaporation-induced method from 14% w/w SEBS solutions in THF/DMF mixtures. (a) 1D scattering profiles of the final films (black symbols) and corresponding fitting curves using the LAM structural model [33] (red dashed lines), each profile is labelled by the THF/DMF mixture composition used for the film preparation. Representative standard deviation bars are shown for the SAXS patterns associated with THF/DMF = 100/0 w/w. For clarity purposes, the 1D SAXS patterns have been multiplied by a factor indicated on the right-hand side of the plot. (b) Corresponding lamellar period (D) and PS sublayer thickness (T) with their standard deviations and the PEB sublayer thickness ($D - T$) calculated from SAXS patterns using the LAM structural model. (c) Cartoon illustration of the self-assembled structure of SEBS in films for THF/DMF = 100/0 w/w. (d) Cartoon illustration of the self-assembled structure of SEBS in films for THF/DMF = 90/10 w/w - 50/50 w/w.

3.3. Self-assembled structure transitions during the SEBS film formation from a solution

To further our understanding of the self-assembled structural transitions from solution to film, time-resolved SAXS measurements were firstly used to follow the dynamics during the THF evaporation process (**Fig. 3a**). For 10 h of THF evaporation, the SEBS sample demonstrated scattering patterns corresponding to dissolved polymer chains (**Fig. 3a**). After 17 h of evaporation a broad peak appeared at $q = 0.22 \text{ \AA}^{-1}$ indicating that phase separation of SEBS occurred. However, this single broad peak provides unclear structural information of the potential SEBS phase separation. However, the orientation of the phase separation structure may provide more information about the condition during the THF evaporation process, and herein, Herman's orientation factor [60-62] at $q = 0.0185 \text{ \AA}^{-1}$ (**Fig. 3b**) is introduced to represent such structural orientation. Meanwhile, the potential lattice period is estimated by $2\pi/q^*$. Between 17 h and 30 h of the THF evaporation process, the estimated lattice period was increasing with the relatively stable Herman's orientation factor, approximately equal to 0.5, possibly indicating of the homogeneous nucleation of the SEBS Gaussian chains. After 27.5 h of evaporation, two diffraction peaks with q/q^* of 1:2 were observed indicating that the SEBS phase-separated structure might begin to form sublayers stacked in a periodic lamellar structure (**Fig. S2**), but the clear lamellar phase with $D = 33.4 \pm 3.0 \text{ nm}$ and $T = 12.2 \pm 2.7 \text{ nm}$, measured using the LAM structural model fitting to the SAXS patterns, was observed at 30.0 h. Then, from 31.0 h to 35.0 h of the solvent evaporation, T remained at 11.6 nm while D increased from $34.0 \pm 2.0 \text{ nm}$ to $36.3 \pm 1.8 \text{ nm}$. The increase of both $(D - T)$ and Herman orientation factor (**Fig. 3b**) indicate that SEBS gradually formed a relatively well-defined oriented LAM structure. However, from 35.0 h to 39.0 h, T

decreased from 11.3 ± 1.6 nm to 10.3 ± 1.7 nm, and D reduced from 36.3 ± 1.6 nm to 35.2 ± 1.7 nm. Therefore, the $(D - T)$ value remained around 25.0 nm, while the Herman's orientation factor reduced from 0.639 to 0.602. The $(D - T)$ values during this period indicated that the PEB sublayers were relatively stable, because they were close to $R_{F_PEB} = 24.3$ nm when $\nu = 0.5$. The reducing T between 35.0 h and 39.0 h indicated that PS blocks become interlocked during the THF vapor annealing process (**Fig. 3a**). Since THF has preference for PS blocks according to the χ values of THF-PS and THF-PEB, significantly more THF might be captured in PS sublayer regions rather than PEB sublayer regions when the THF evaporation process approached its completion. Therefore, the THF evaporation at this stage affected sufficiently the interdigitating of PS coils. Also, fast THF evaporation introduced defects during the self-assembling process towards film formation, as observed by the decrease of the Herman's orientation factor between 35.0 h and 39.0 h. From 39.0 h to 42.0 h, T remained around 10.0 nm, and the $(D - T)$ value slightly decreased from 24.9 nm to 24.3 nm. Furthermore, PEB blocks were shown to be stretched to Gaussian chains, estimated by $(D - T)$ due to $R_{F_PEB} = 24.3$ nm when $\nu = 0.5$. Finally, after 42.0 h, when D , T , and the Herman orientation factor were remained virtually constant the formation of SEBS self-assembled structure was complete.

as a green dot. (b) Evolution of lamellar period (D) (red down-pointing triangles), PS sublayer thickness (T) (blue squares), PEB sublayer thickness ($D - T$) (purple up-pointing triangles), and the Herman orientation factor (open red diamonds) with time recorded during the evaporation. The error bars correspond to the standard deviations of D and $D - T$.

Similarly, the nanostructure transformation of the evaporation-induced SEBS film preparation in THF/DMF = 80/20 w/w at 14% w/w was monitored by SAXS (**Fig. 4a-b**). These 1D and 2D SAXS patterns indicate that the nanostructure transition of SEBS in this cosolvent composition was more complex than in pure THF (**Figure 3**), and the first three or four clear peak positions and the corresponding peak position ratios are highlighted to demonstrate this nanostructure transformation (**Fig. 4c-d**). From 0 to 27.5 h, there was no obvious change of q^* , and the peak position ratios of q_2/q^* , q_3/q^* , and q_4/q^* were 1.5, 2.4, 3.5, respectively. The calculated ratios indicate that the SEBS copolymers formed an FCC structure where $q^*:q_2:q_3:q_4$ was approximately $1:\sqrt{8/3}:\sqrt{20/3}:\sqrt{35/3}$. From 27.5 to 39 h, q^* peak position continuously decreased, while q_2 , q_3 , and q_4 also shifted towards lower q values. During this time interval, the peak position ratios of q_2/q^* , q_3/q^* , and q_4/q^* were 1.2, 2.4, and 3.5, respectively. The obtained ratios suggest that SEBS formed a BCC structure where $q_1:q_2:q_3:q_4$ was approximately $1:\sqrt{2}:\sqrt{7}:\sqrt{13}$. After 35 h, the BCC sphere radius was 18.0 nm (**Fig. S3**) and the lattice period was estimated to be 72.9 nm, which indicates that the packing density of this BCC structure was 16.6%. The packing density has slightly increased from 16.2% calculated for SEBS in the FCC structure after 30 h. The possible reason for this FCC-to-BCC transformation might be the sample compression perpendicular to the SEBS film plane [63]. After 40 h, the SEBS nanostructure transformed into a hexagonally packed cylinder morphology where $q^*:q_2:q_3:q_4$ was approximately $1:2:\sqrt{13}:\sqrt{21}$, corresponding to 100,

200, 310 and 410 diffraction peaks of a hexagonal close-packed (HCP) cylinder structure [64]. Since the 210 diffraction peak at around 0.035 \AA^{-1} partially overlaps with the 200 diffraction peak (**Fig. 4a**), the 210 peak was not labelled and the peak at $q \sim 0.46 \text{ \AA}^{-1}$ (q_3 peak) was assigned to 310 Miller indexes. The cylinder cross section radius was estimated to be 18.5 nm (**Fig. S3**) which was close to the PS sphere radius within the previously adopted BCC structure. This value together with 47.2 nm inter-plane spacing for the 100 diffraction peak suggest that the packing density of the close-packed cylinders was 35.1%, which matches the volume fraction of PS in SEBS. After 40 h of the solvent evaporation the peak position ratios of q_2/q^* and q_3/q^* changed to 2.0 and 3.0, respectively, revealing the formation of a lamellae nanostructure. No further nanostructure transformations were observed during the SAXS data collection. The HCP-to-LAM transformation also indicated that the fusion of PS hexagonally packed cylinders forced the folded PEB blocks to form LAM structure (**Fig. 2**). The kinetic of HCP-to-LAM transformation can be described by the clear peak position ratio change of q_3/q^* and then estimated Avrami equation [65-68] for q_3/q^* as $q_3/q^*(t) = q_3/q^*(t_\infty) + A \cdot \exp[-t^n / \tau]$, where $q_3/q^*(t)$ is the time-dependent q_3/q^* value, t is time, A is a temperature-dependent constant, n is Avrami exponent, and τ is characteristic time. The fitting of q_3/q^* via Avrami equation, $q_3/q^*(t) = 2.91 + 1.70 \times 10^6 \cdot \exp(-t^{1.00} / 2.71)$, with $n = 1.00$ indicates that the HCP to LAM transformation is a interface-controlled phase transition.

As self-consistent field theory (SCFT) prediction of symmetric ABA triblock copolymer melts, the bridged configurations (**Fig. 2c**) of the ABA triblock copolymers are about 40%–45% [59]. However, the bridged configurations were dominant for no DMF (THF/DMF = 100/0 w/w), but the loops configurations (**Fig. 2d**) were dominant when the solutions were contained DMF. With time-resolved SAXS studies, it observed that the SEBS self-assembled transformations depended not only on the χ values between PS and PEB blocks and the R_g s of the PS and PEB blocks but

also on the gradually increased SEBS concentrations and remained (co)solvents. Therefore, the nanofabrication method could affect the block copolymer configurations.

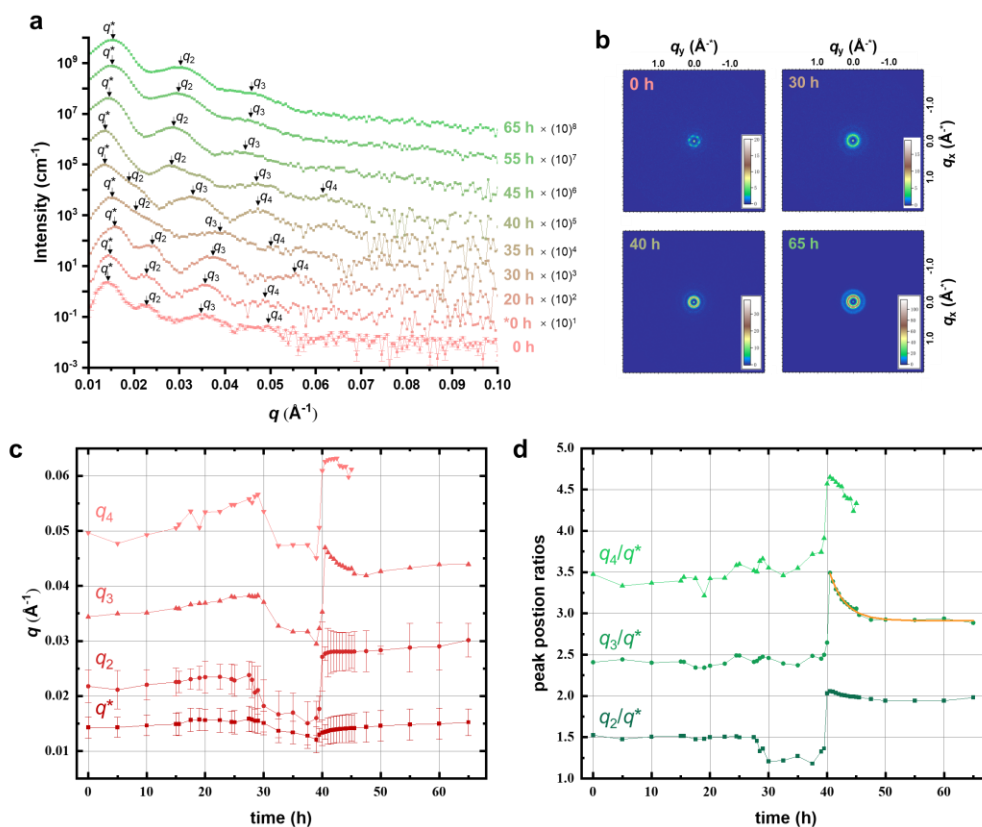


Fig. 4. SAXS analysis of the evaporation-induced film formation from 14% w/w SEBS solution in THF/DMF = 80/20 w/w. (a) Selected time-resolved 1D SAXS patterns recorded during the evaporation. Corresponding multiplication factors used to shift the scattering curves on the plot for the sake of clarity and evaporation times are shown at the top of each profile. Representative intensity error bars are shown for SAXS pattern associated with 0 h. First three or four resolved diffraction peaks (q^* , q_2 , q_3 , and q_4) are labeled on the SAXS patterns. (b) Representative 2D SAXS patterns recorded *in situ* during the evaporation-induced SEBS film preparation. (c) Peak (q^* , q_2 , q_3 , and q_4) positions measured from the time-resolved 1D SAXS patterns. The error bars provided for the q^* and q_2 peaks show full width at half maximum of the peaks. (d) Peak position ratios (q_2/q^* , q_3/q^* , and q_4/q^*) calculated from the SAXS patterns. The kinetic of HCP to LAM

transformation can be estimated by Avrami equation for q_3/q^* labeled with the fitting result, $q_3/q^*(t) = 2.91 + 1.70 \times 10^6 \cdot \exp(-t^{1.00} / 2.71)$ (solid orange line).

3.4. Self-assembled structure of SEBS electrospun fiber and self-assembled structure transitions from SEBS electrospun fiber to SEBS film

To compare the self-assembled nanostructure adopted by SEBS fibers with the SAXS measurements obtained during annealing via the evaporation-induced method, electrospun or electrospayed products were prepared from SEBS solutions of 14% w/w in THF/DMF = 100/0, 90/10, 80/20, 70/30, 60/40, and 50/50 w/w, respectively (**Fig. S4**). However, according to the SEM results (**Fig. S4**), only SEBS product prepared in THF/DMF = 100/0 was fiber formation. According to the discussion above of the SEBS film formation from a solution, SEBS chains primarily formed FCC and LAM structures in cosolvents, and the SEBS chains were folded in looped configurations to form the diblock copolymer formations in the final products (**Fig. 2**). This indicated that the degradation of the SEBS triblock copolymer into a diblock copolymer formation might lead to a reduction in the SEBS chain entanglements (**Fig. S4**), and therefore, the electrospun or electrospayed products of SEBS solutions in THF/DMF mixtures cannot produce well-defined fiber formation. Accordingly, only SEBS product prepared in THF/DMF = 100/0 can be used for further time-resolved SAXS studies of THF vapor annealing of SEBS electrospun fibers.

The THF vapor annealing of SEBS electrospun fibers was recorded by time-resolved SAXS (**Fig. 5a-b**). While the scattering intensities from $q = 0.005$ to $q = 0.015 \text{ \AA}^{-1}$ might be contributed by orient electrospun fibers, the time-resolved SAXS cannot be independently fitted by the LAM structural model [33] (**Fig. 5b**). Thus, the LAM modelling only focused on from $q = 0.015$ to $q = 0.10 \text{ \AA}^{-1}$, and therefore, only the lamellar period (D) (**Fig. 5d**) of LAM modelling results were reliable, while the PS sublayer thickness (T) (**Fig. 5d**) can only be treated as circumstantial

evidence. Since 75 min, there was no obviously LAM structure observed by LAM structural model, and from 77 min, no notably SAXS pattern was detected (**Fig. 5a-b**). Meanwhile, the orientation of electrospun fibers and the LAM structures (**Fig. 5a**) can be observed the Herman's orientation factor at $q = 0.006 \text{ \AA}^{-1}$ and $q = 0.023 \text{ \AA}^{-1}$ (**Fig. 5c**), respectively. These two orientation indexes about the macro- and nano-structural information can possibly provide more evidence about the morphological transition of the electrospun fibers.

According to SAXS patterns, the primary SEBS electrospun fibers already contained LAM structure of $D = 19.14 \pm 0.44 \text{ nm}$, and after 2 min of THF vapor annealing, D increased to $24.29 \pm 1.18 \text{ nm}$, which is close to $R_{F_PEB} = 24.3 \text{ nm}$ when $\nu = 0.5$. Interestingly, D continuously increased $28.61 \pm 0.13 \text{ nm}$ at 18 min, and then gradually decreased to $26.41 \pm 0.02 \text{ nm}$ at 73 min. With T as references, in the primary SEBS electrospun fibers, D and T were nearly the same, which implied that the PS blocks of different SEBS chains might be aggregated, possibly due to the fast THF solvent evaporation, and thus, the PEB blocks were compressed (**Fig. 5e-i**). Once THF vapor annealing process occurred, the aggregations PS blocks of different SEBS chains separated and the compressed PEB blocks were relaxed (**Fig. 5e-ii**). T mainly declined in the first 20 min and then remained around 12 nm from 20 min to 60 min, which was close to $4R_{g_PS} (= 11.5 \text{ nm})$.

Since the SEBS electrospun fiber was collected onto a cage rotor with 2200 rpm [24], the SEBS fiber remained relatively high level orientation with 10 min characterized by the Herman's orientation factor at $q = 0.006 \text{ \AA}^{-1}$ (**Fig. 5c**). From 10 to 20 min, the Herman's orientation factor at $q = 0.006 \text{ \AA}^{-1}$ reduced, possibly because the sticky SEBS fibers were stained together [24]. The Herman's orientation factor at $q = 0.023 \text{ \AA}^{-1}$ (**Fig. 5d**), representing the level of the LAM structure orientation, gradually increased to the same orientation level as the fibers at 60 min. Meanwhile

with 2D SAXS pattern at 60 min (**Fig. 5a**), the orientations of the LAM structure and fiber were the same.

From 60 to 77 min, T gradually increased from 12.6 ± 4.8 nm to 16.4 ± 8.2 nm, which might suggest that the interdigitated PS blocks were gradually detached by the increasing amount of THF vapor invaded in the SEBS electrospun fibers (**Fig. 5e-iii**). At 77 min, the invaded THF vapor nearly fully broke the physical cross-linking constructed by the PS block domains, and thus, the well-ordered lamellae nanostructure broke into fractions and the SEBS electrospun fibers totally collapsed.

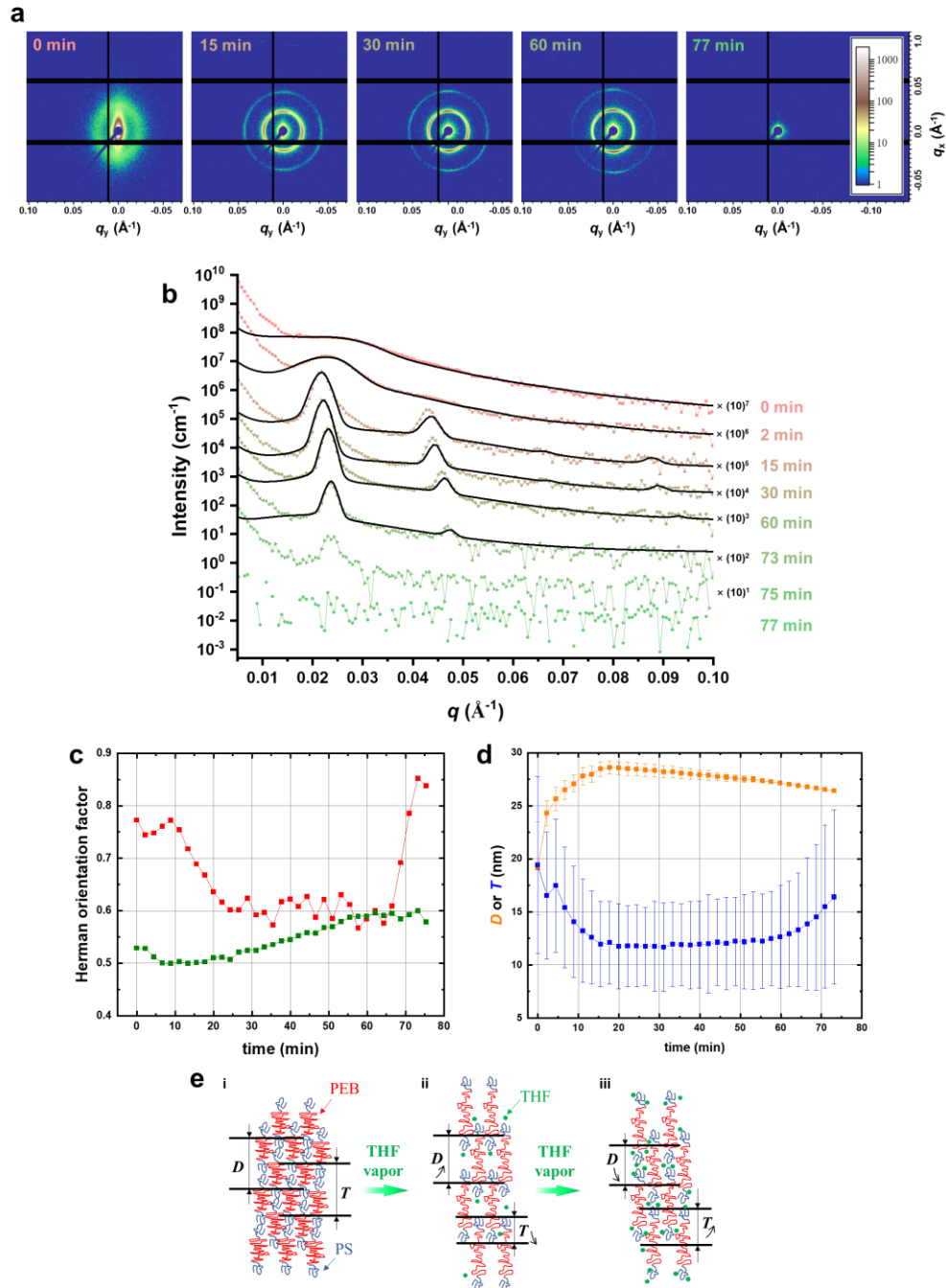


Fig. 5. (a) 2D SAXS patterns collected during THF vapor-annealing of electrospun SEBS fibers after 0, 15, 30, 60, and 75 min. (b) Time-resolved 1D SAXS patterns recorded during THF vapor-annealing of electrospun SEBS fibers after 0, 2, 15, 30, 60, 73, 75, and 77 min. The corresponding fits (solid black curves) were obtained using the LAM structural model [33]. The 1D SAXS patterns are shifted by a factor labeled beside the patterns, for the sake of clarity. (c) Herman's orientation factor at $q = 0.006 \text{ \AA}^{-1}$ (red squares) and at $q = 0.023 \text{ \AA}^{-1}$ (green squares) during THF

vapor-annealing of electrospun SEBS fibers from 0 to 75 min. (d) Sublayer thickness (T) with standard deviation (blue squares) and inter-plane distances (D) (orange squares) with standard deviation of the LAM structure vs time recorded during THF vapor-annealing of electrospun SEBS fibers from 0 to 73 min. (e) Structure illustrations of the LAM structural morphological transitions via THF vapor-annealing. PEB is represented as a red coil, PS is represented as a blue coil, and THF molecule is represented as a green dot. I stage represents the primary LAM structure of the SEBS electrospun fibers. II stage represents the LAM structure before SEBS electrospun fibers collapsed. III stage represents the LAM structure during the collapse of the SEBS electrospun fibers collapsed.

4. Conclusion

SEBS triblock copolymer macromolecules in THF have been shown to adopt Gaussian chains. During the evaporation-induced method, SEBS forms a LAM morphology, as confirmed by time-resolved SAXS measurements, with PS coils with head-to-head configuration. However, by adding DMF in the system to form THF/DMF cosolvents, SEBS can form FCC self-assembled structures in addition to LAM with two PS coils with head-to-head configuration. However, SAXS measurements suggest that in LAM prepared in the THF/DMF cosolvent systems, PEB blocks in such LAM are always folded. Time-resolved SAXS measurements indicated that SEBS sequentially forms FCC, BCC, HCP, and LAM self-assembled structures in THF/DMF = 80/20 w/w. Also, time-resolved SAXS measurements suggest that the folded SEBS in LAM formed by evaporation-induced method in THF/DMF = 80/20 w/w were constructed when PS blocks fused during the HCP-to-LAM transition, which indicated that such transition could induce the folded PEB blocks in final LAM products. To establish an example of SEBS film forming the confined SEBS chains, electrospinning was utilized. SAXS measurements indicate that the electrospun

SEBS fibers contain LAM structure, and time-resolved SAXS measurements suggest that the LAM morphology formed via the electrospinning preparation method comprise from interdigitated PS blocks rather than head-to-head PS sublayer structure. This finding of the self-assembled SEBS structures in electrospun fibers and structure transition during vapor annealing can inspire the design of electrospun fibers to improve their mechanical properties. The SEBS film prepared under the unconfined and confined situations indicates that the preparation methods are significantly critical to the self-assembled block copolymer structures. However, the (co)solvent effects and the conformations of SEBS triblock copolymers still influence the precise self-assembled structures formed in unconfined or confined environments.

CRedit authorship contribution statement

Guoxing Liao: Methodology, Validation, Formal analysis, Investigation, Data curation, Writing - original draft, Writing, review & editing. **Lei Chen:** Methodology, Validation, Formal analysis, Investigation, Data curation, Writing - original draft. **Yunjie Zhang:** Formal analysis, Investigation, Data curation. **Oleksandr O. Mykhaylyk:** validation, Data curation, writing, review and editing. **Paul D. Topham:** Validation, Writing, review & editing. **Daniel T. W. Toolan:** Validation, Formal analysis. **Matthew J. Derry:** Validation, Writing, review & editing. **Jonathan R. Howse:** Validation, Formal analysis. **Qianqian Yu:** Validation, Formal analysis. **Guiju Feng:** Validation, Formal analysis. **LinGe Wang:** Conceptualization, Methodology, Data curation, Resources, Writing - review & editing, Supervision, Funding acquisition.

Declaration of competing interest

The authors declare that they have no known competing financial interests or personal relationships that could have appeared to influence the work reported in this paper.

Acknowledgments

The authors thank the financial support from the National Natural Science Foundation of China (No. 51890871 and U22A20316), Guangdong Province Basic and Applied Basic Research Fund Project (2023A1515012013), Recruitment Program of Guangdong (No. 2016ZT06C322), Science and Technology Program of Guangzhou (No. 2023B03J0037) and Overseas Expertise Introduction Center for Discipline Innovation (“111 Center”).

References

- [1] J.Y. Cheng, A.M. Mayes, C.A. Ross, Nanostructure engineering by templated self-assembly of block copolymers, *Nature materials* 3(11) (2004) 823-828.
- [2] Y. Mai, A. Eisenberg, Self-assembly of block copolymers, *Chemical Society Reviews* 41(18) (2012) 5969-5985.
- [3] M. Stefik, S. Guldin, S. Vignolini, U. Wiesner, U. Steiner, Block copolymer self-assembly for nanophotonics, *Chemical Society Reviews* 44(15) (2015) 5076-5091.
- [4] M. Robertson, Q. Zhou, C. Ye, Z. Qiang, Developing Anisotropy in Self-Assembled Block Copolymers: Methods, Properties, and Applications, *Macromolecular Rapid Communications* 42(17) (2021) 2100300.
- [5] A. Alvarez-Fernandez, C. Cummins, M. Saba, U. Steiner, G. Fleury, V. Ponsinet, S. Guldin, Block copolymer directed metamaterials and metasurfaces for novel optical devices, *Advanced Optical Materials* 9(16) (2021) 2100175.
- [6] C.T. Black, R. Ruiz, G. Breyta, J.Y. Cheng, M.E. Colburn, K.W. Guarini, H.C. Kim, Y. Zhang, Polymer self assembly in semiconductor microelectronics, *IBM Journal of Research and Development* 51(5) (2007) 605-633.

- [7] Z. Ge, S. Liu, Functional block copolymer assemblies responsive to tumor and intracellular microenvironments for site-specific drug delivery and enhanced imaging performance, *Chemical Society Reviews* 42(17) (2013) 7289-7325.
- [8] T. Yun, H.M. Jin, D.H. Kim, K.H. Han, G.G. Yang, G.Y. Lee, G.S. Lee, J.Y. Choi, I.D. Kim, S.O. Kim, 2D metal chalcogenide nanopatterns by block copolymer lithography, *Advanced Functional Materials* 28(50) (2018) 1804508.
- [9] E.A. Jackson, M.A. Hillmyer, Nanoporous membranes derived from block copolymers: from drug delivery to water filtration, *ACS nano* 4(7) (2010) 3548-3553.
- [10] C. Cummins, R. Lundy, J.J. Walsh, V. Ponsinet, G. Fleury, M.A. Morris, Enabling future nanomanufacturing through block copolymer self-assembly: A review, *Nano Today* 35 (2020) 100936.
- [11] J.N.L. Albert, T.H. Epps, Self-assembly of block copolymer thin films, *Materials Today* 13(6) (2010) 24-33.
- [12] J.M.G. Swann, P.D. Topham, Design and Application of Nanoscale Actuators Using Block-Copolymers, *Polymers* 2(4) (2010) 454-469.
- [13] H.-A. Klok, S. Lecommandoux, Supramolecular Materials via Block Copolymer Self-Assembly, *Advanced Materials* 13(16) (2001) 1217-1229.
- [14] C. Jin, B.C. Olsen, E.J. Luber, J.M. Buriak, Nanopatterning via solvent vapor annealing of block copolymer thin films, *Chemistry of Materials* 29(1) (2017) 176-188.
- [15] K. Aissou, M. Mumtaz, G. Portale, C. Brochon, E. Cloutet, G. Fleury, G. Hadziioannou, Templated Sub-100-nm-Thick Double-Gyroid Structure from Si-Containing Block Copolymer Thin Films, *Small* 13(20) (2017) 1603777.
- [16] L. Chen, S. Wang, Q. Yu, P.D. Topham, C. Chen, L. Wang, A comprehensive review of electrospinning block copolymers, *Soft Matter* 15(12) (2019) 2490-2510.
- [17] S.J. Cho, S.M. Jung, M. Kang, H.S. Shin, J.H. Youk, Preparation of hydrophilic PCL nanofiber scaffolds via electrospinning of PCL/PVP-b-PCL block copolymers for enhanced cell biocompatibility, *Polymer* 69 (2015) 95-102.
- [18] K.W. Gotrik, C. Ross, Solvothermal annealing of block copolymer thin films, *Nano letters* 13(11) (2013) 5117-5122.
- [19] C. Park, J. Yoon, E.L. Thomas, Enabling nanotechnology with self assembled block copolymer patterns, *Polymer* 44(22) (2003) 6725-6760.
- [20] M.A. Chavis, D.M. Smilgies, U.B. Wiesner, C.K. Ober, Widely tunable morphologies in block copolymer thin films through solvent vapor annealing using mixtures of selective solvents, *Advanced functional materials* 25(20) (2015) 3057-3065.
- [21] E. Kim, S. Park, Y.-S. Han, T.-H. Kim, Effect of solvent selectivity on supramolecular assemblies of block copolymer by solvent-vapor annealing, *Polymer* 150 (2018) 214-222.
- [22] M. Trejo-Maldonado, A. Womiloju, S. Stumpf, S. Hoepfner, U.S. Schubert, L.E. Elizalde, C. Guerrero-Sanchez, Triazole-Functionalized Mesoporous Materials Based on Poly (styrene-block-lactic acid): A Morphology Study of Thin Films, *Polymers* 14(11) (2022) 2231.
- [23] A. Alvarez-Fernandez, M.J. Fornerod, B. Reid, S. Guldin, Solvent vapor annealing for controlled pore expansion of block copolymer-assembled inorganic mesoporous films, *Langmuir* 38(10) (2022) 3297-3304.
- [24] L. Chen, Q. Yu, Y. Jia, M. Xu, Y. Wang, J. Wang, T. Wen, L. Wang, Micro-and-nanometer topological gradient of block copolymer fibrous scaffolds towards region-specific cell regulation, *Journal of Colloid and Interface Science* 606 (2022) 248-260.

- [25] J.M. Shin, Y.J. Lee, M. Kim, K.H. Ku, J. Lee, Y. Kim, H. Yun, K. Liao, C.J. Hawker, B.J. Kim, Development of shape-tuned, monodisperse block copolymer particles through solvent-mediated particle restructuring, *Chemistry of Materials* 31(3) (2019) 1066-1074.
- [26] L.-C. Cheng, W. Bai, E.F. Martin, K.-H. Tu, K. Ntetsikas, G. Lontos, A. Avgeropoulos, C. Ross, Morphology, directed self-assembly and pattern transfer from a high molecular weight polystyrene-block-poly (dimethylsiloxane) block copolymer film, *Nanotechnology* 28(14) (2017) 145301.
- [27] T. Ghoshal, A. Chaudhari, C. Cummins, M.T. Shaw, J.D. Holmes, M.A. Morris, Morphological evolution of lamellar forming polystyrene-block-poly (4-vinylpyridine) copolymers under solvent annealing, *Soft Matter* 12(24) (2016) 5429-5437.
- [28] X. Shi, Z. Xu, C. Huang, Y. Wang, Z. Cui, Selective swelling of electrospun block copolymers: from perforated nanofibers to high flux and responsive ultrafiltration membranes, *Macromolecules* 51(6) (2018) 2283-2292.
- [29] M. Cetintas, M. Kamperman, Self-assembly of PS-b-PNIPAM-b-PS block copolymer thin films via selective solvent annealing, *Polymer* 107 (2016) 387-397.
- [30] Y.S. Jung, C.A. Ross, Solvent-Vapor-Induced Tunability of Self-Assembled Block Copolymer Patterns, *Advanced Materials* 21(24) (2009) 2540-2545.
- [31] C. Sinturel, M. Vayer, M. Morris, M.A. Hillmyer, Solvent vapor annealing of block polymer thin films, *Macromolecules* 46(14) (2013) 5399-5415.
- [32] C. Stegelmeier, A. Exner, S. Hauschild, V. Filiz, J. Perlich, S.V. Roth, V. Abetz, S. Förster, Evaporation-Induced Block Copolymer Self-Assembly into Membranes Studied by in Situ Synchrotron SAXS, *Macromolecules* 48(5) (2015) 1524-1530.
- [33] L. Wang, P.D. Topham, O.O. Mykhaylyk, H. Yu, A.J. Ryan, J.P.A. Fairclough, W. Bras, Self-Assembly-Driven Electrospinning: The Transition from Fibers to Intact Beaded Morphologies, *Macromolecular rapid communications* 36(15) (2015) 1437-1443.
- [34] J. Wu, X. Li, Y. Wu, G. Liao, P. Johnston, P.D. Topham, L. Wang, Rinse-resistant superhydrophobic block copolymer fabrics by electrospinning, electro spraying and thermally-induced self-assembly, *Applied Surface Science* 422 (2017) 769-777.
- [35] M. Sztucki, SAXSutilities2: a Graphical User Interface For Processing and Analysis of Small-Angle X-ray Scattering Data, Zenodo, 2021.
- [36] S. Förster, L. Apostol, W. Bras, Scatter: software for the analysis of nano- and mesoscale small-angle scattering, *Journal of Applied Crystallography* 43(3) (2010) 639-646.
- [37] J. Ilavsky, P.R. Jemian, Irena: tool suite for modeling and analysis of small-angle scattering, *Journal of Applied Crystallography* 42(2) (2009) 347-353.
- [38] B.D. Gates, Q. Xu, M. Stewart, D. Ryan, C.G. Willson, G.M. Whitesides, New approaches to nanofabrication: molding, printing, and other techniques, *Chemical reviews* 105(4) (2005) 1171-1196.
- [39] M.H. Lee, M.D. Huntington, W. Zhou, J.-C. Yang, T.W. Odom, Programmable soft lithography: solvent-assisted nanoscale embossing, *Nano letters* 11(2) (2011) 311-315.
- [40] Y. Lu, S. Chen, Micro and nano-fabrication of biodegradable polymers for drug delivery, *Advanced drug delivery reviews* 56(11) (2004) 1621-1633.
- [41] P. Pula, A. Leniart, P.W. Majewski, Solvent-assisted self-assembly of block copolymer thin films, *Soft Matter* 18(21) (2022) 4042-4066.
- [42] S. Abbott, C.M. Hansen, Hansen solubility parameters in practice, Hansen-Solubility2008.
- [43] C.M. Hansen, Hansen solubility parameters: a user's handbook, CRC press2007.

- [44] A.F. Barton, CRC handbook of solubility parameters and other cohesion parameters, Routledge, Boca Raton, 2017.
- [45] T. Lindvig, M.L. Michelsen, G.M. Kontogeorgis, A Flory–Huggins model based on the Hansen solubility parameters, *Fluid Phase Equilibria* 203(1-2) (2002) 247-260.
- [46] T.L. Chantawansri, A.J. Duncan, J. Ilavsky, K.K. Stokes, M.C. Berg, R.A. Mrozek, J.L. Lenhart, F.L. Beyer, J.W. Andzelm, Phase behavior of SEBS triblock copolymer gels, *Journal of Polymer Science Part B: Polymer Physics* 49(20) (2011) 1479-1491.
- [47] B. Hammouda, SANS from homogeneous polymer mixtures: a unified overview, *Polymer Characteristics*, Springer 1993, pp. 87-133.
- [48] S. Förster, A. Timmann, M. Konrad, C. Schellbach, A. Meyer, S.S. Funari, P. Mulvaney, R. Knott, Scattering Curves of Ordered Mesoscopic Materials, *The Journal of Physical Chemistry B* 109(4) (2005) 1347-1360.
- [49] M.O. Tuhin, J.J. Ryan, J.D. Sadler, Z. Han, B. Lee, S.D. Smith, M.A. Pasquinelli, R.J. Spontak, Microphase-Separated Morphologies and Molecular Network Topologies in Multiblock Copolymer Gels, *Macromolecules* 51(14) (2018) 5173-5181.
- [50] T.H. Epps, E.W. Cochran, T.S. Bailey, R.S. Waletzko, C.M. Hardy, F.S. Bates, Ordered Network Phases in Linear Poly(isoprene-*b*-styrene-*b*-ethylene oxide) Triblock Copolymers, *Macromolecules* 37(22) (2004) 8325-8341.
- [51] K. Reynders, N. Mischenko, R. Kleppinger, H. Reynaers, M.H.J. Koch, K. Mortensen, Ordering Phenomena in ABA Triblock Copolymer Gels, *Journal of Applied Crystallography* 30(5-2) (1997) 684-689.
- [52] K. Hashimoto, M. Hirasawa, H. Kokubo, R. Tamate, X. Li, M. Shibayama, M. Watanabe, Transport and Mechanical Properties of ABA-type Triblock Copolymer Ion Gels Correlated with Their Microstructures, *Macromolecules* 52(21) (2019) 8430-8439.
- [53] I.W. Hamley, C. Daniel, W. Mingvanish, S.-M. Mai, C. Booth, L. Messe, A.J. Ryan, From Hard Spheres to Soft Spheres: The Effect of Copolymer Composition on the Structure of Micellar Cubic Phases Formed by Diblock Copolymers in Aqueous Solution, *Langmuir* 16(6) (2000) 2508-2514.
- [54] G.A. McConnell, M.Y. Lin, A.P. Gast, Long Range Order in Polymeric Micelles under Steady Shear, *Macromolecules* 28(20) (1995) 6754-6764.
- [55] Y.-Y. Huang, J.-Y. Hsu, H.-L. Chen, T. Hashimoto, Existence of fcc-Packed Spherical Micelles in Diblock Copolymer Melt, *Macromolecules* 40(3) (2007) 406-409.
- [56] N. Sakamoto, T. Hashimoto, C.D. Han, D. Kim, N.Y. Vaidya, Order–Order and Order–Disorder Transitions in a Polystyrene-block-Polyisoprene-block-Polystyrene Copolymer, *Macromolecules* 30(6) (1997) 1621-1632.
- [57] N. Sakamoto, T. Hashimoto, Ordering Dynamics of Cylindrical and Spherical Microdomains in Polystyrene-block-Polyisoprene-block-Polystyrene. 1. SAXS and TEM Observations for the Grain Formation, *Macromolecules* 31(24) (1998) 8493-8502.
- [58] A.S. Krishnan, S.D. Smith, R.J. Spontak, Ternary Phase Behavior of a Triblock Copolymer in the Presence of an Endblock-Selective Homopolymer and a Midblock-Selective Oil, *Macromolecules* 45(15) (2012) 6056-6067.
- [59] M.W. Matsen, R.B. Thompson, Equilibrium behavior of symmetric ABA triblock copolymer melts, *The Journal of Chemical Physics* 111(15) (1999) 7139-7146.
- [60] P. Hermans, Principles of the mathematical treatment of constant-pressure filtration, *J. Soc. Chem. Ind.* 55 (1936) 1.

- [61] J. Hermans, P. Hermans, D. Vermaas, A. Weidinger, Quantitative evaluation of orientation in cellulose fibres from the X-ray fibre diagram, *Recueil des Travaux Chimiques des Pays-Bas* 65(6) (1946) 427-447.
- [62] P. Hermans, A. Weidinger, Quantitative X-ray investigations on the crystallinity of cellulose fibers. A background analysis, *Journal of Applied Physics* 19(5) (1948) 491-506.
- [63] C. Engin, H.M. Urbassek, Molecular-dynamics investigation of the fcc→bcc phase transformation in Fe, *Computational Materials Science* 41(3) (2008) 297-304.
- [64] T.A. Mykhaylyk, O.O. Mykhaylyk, S. Collins, I.W. Hamley, Ordered Structures and Phase Transitions in Mixtures of a Polystyrene/Polyisoprene Block Copolymer with the Corresponding Homopolymers in Thin Films and in Bulk, *Macromolecules* 37(9) (2004) 3369-3377.
- [65] Y. Liu, M. Li, R. Bansil, M. Steinhart, Kinetics of Phase Transition from Lamellar to Hexagonally Packed Cylinders for a Triblock Copolymer in a Selective Solvent, *Macromolecules* 40(26) (2007) 9482-9490.
- [66] M. Li, Y. Liu, H. Nie, R. Bansil, M. Steinhart, Kinetics of Hexagonal–Body-Centered Cubic Transition in a Triblock Copolymer in a Selective Solvent: Time-Resolved Small-Angle X-ray Scattering Measurements and Model Calculations, *Macromolecules* 40(26) (2007) 9491-9502.
- [67] H. Nie, R. Bansil, K. Ludwig, M. Steinhart, Č. Koňák, J. Bang, Time-Resolved Small-Angle X-ray Scattering Study of the Kinetics of Disorder–Order Transition in a Triblock Copolymer in a Selective Solvent for the Middle Block, *Macromolecules* 36(21) (2003) 8097-8106.
- [68] M. Avrami, Kinetics of Phase Change. I General Theory, *The Journal of Chemical Physics* 7(12) (1939) 1103-1112.